

Positron scattering from atoms and molecules using a magnetized beam

J. P. Sullivan, S. J. Gilbert, J. P. Marler, R. G. Greaves,* S. J. Buckman,† and C. M. Surko
Department of Physics, University of California, San Diego, 9500 Gilman Drive, La Jolla, California 92093-0319
 (Received 7 January 2002; published 15 October 2002)

The development of buffer-gas trapping and magnetized beam formation has provided positron beams with significantly improved energy resolution ($\Delta E \leq 0.025$ eV) compared to those available previously. Analysis techniques have been developed to take advantage of the fact that the beam is in a magnetic field of ~ 0.1 T. This has enabled scattering experiments at lower energies and with significantly improved state selectivity for excitation experiments than had been possible previously. A detailed description of these techniques is presented. Data are presented for a variety of cross sections for scattering of positrons from atomic and molecular targets.

DOI: 10.1103/PhysRevA.66.042708

PACS number(s): 34.85.+x, 39.30.+w, 34.50.-s

I. INTRODUCTION

The study of atomic and molecular physics using positrons has been an active area of experimental and theoretical research for many years. Several review articles and books provide an overview of this work [1–8]. The interaction of a positron with matter is an interesting theoretical problem, requiring more than a simple change of charge sign when compared to electron scattering. For instance, the static Coulomb interaction between the target and projectile is attractive for electron scattering and repulsive for positrons, while the dipole polarization is attractive in both cases. The exchange interaction in electron scattering is absent in the case of positron scattering, while positronium formation provides a scattering channel not present in electron scattering. These differences provide challenges to theory when attempting to fully describe the interaction of low-energy positrons with atoms and molecules.

Positrons are increasingly finding importance in such fields as materials science [9], plasma physics [10], and mass spectrometry [11]. Thus, understanding the basic physics underlying positron interactions is important for the development of these areas.

Low-energy positrons for experimental studies have traditionally been obtained from either a radioactive or accelerator-based source, with the positrons then passed through, or reflected from, a moderating material [12]. These moderated beams have an energy width typically ≥ 0.5 eV, depending on the moderating material. The intensities of these beams are quite low compared to typical electron sources, but nonetheless they have been used for extensive experimental studies, such as measurement of ionization [13–16], positronium formation [17–20], many grand total cross sections (see Refs. [4,6,21,22] and references therein), and some differential cross sections [4,23–25]. The resolution of moderated positron sources has limited the energy

range and precision of these pioneering studies, especially for the case of low impact energy, leaving a wide range of positron interactions yet to be fully investigated [26].

With the development of buffer-gas traps, which provide a thermal source of positrons [27], came the opportunity to develop a high-resolution [ΔE as low as 18 meV, full width at half maximum(FWHM)], tunable (~ 0.05 to > 50 eV) positron beam [28,29]. The beam is formed in a magnetic field of ~ 0.1 T. As a consequence, traditional electrostatic approaches to scattering experiments cannot be used. Instead, different scattering techniques have been developed to perform these experiments, which take advantage of the properties of positrons in a high magnetic field. This has enabled further positron experiments and provides the opportunity to investigate unanswered questions concerning the nature of low-energy positron interactions with matter [30–33]. Problems include whether positrons can form bound or quasibound states (resonances) with atomic and molecular targets. Such states have been proposed to explain large annihilation rates observed in some classes of molecules [34–37]. Another open question is the extent to which the spin-orbit interaction plays a role in positron scattering [38,39]. Finally, the next generation of positron sources for both fundamental experiments and commercial application are likely to rely on buffer gas positron accumulators [27,40]. An accurate knowledge of scattering cross sections provides important information in order to understand the operation of these devices.

This paper presents an overview of the techniques developed to study positron scattering from atoms and molecules by exploiting the properties of the positron orbits in a magnetic field. The experiments are conducted in the limit in which the positron beam is strongly magnetized in the sense that the quantity E_{\perp}/B is an adiabatic invariant, where E_{\perp} is the energy in the positron gyromotion and B is the magnetic field. As we describe below, the use of a magnetic field that varies in strength between the scattering and detection regions and the invariance of E_{\perp}/B enables studies of positron scattering from atomic and molecular targets with a precision unavailable using other methods. Techniques to measure grand total, elastic differential, total inelastic, and total positronium formation cross sections are described. Measurements of these cross sections are presented for a variety of

*Present address: First Point Scientific, Inc., Agoura Hills, CA 91301.

†Present address: Research School of Physical Sciences and Engineering, Australian National University, Canberra, ACT, Australia.

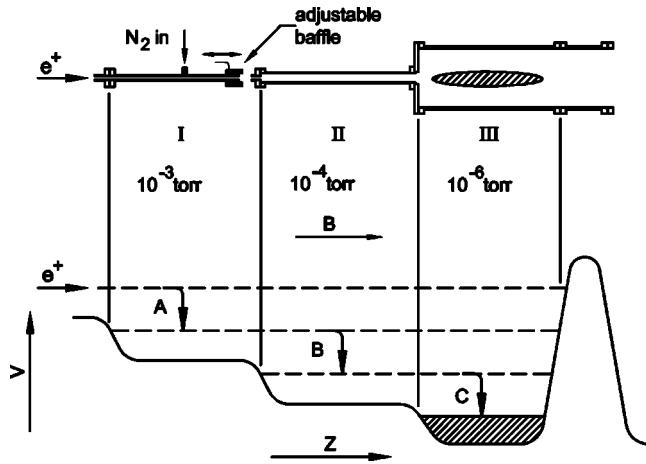


FIG. 1. Above: buffer-gas trap electrode structure; below: typical pressure and voltage profiles as a function of distance z . A, B, and C indicate successive collisions that trap the positrons.

atomic and molecular targets and comparison with previous work and theoretical calculations is made, where possible. Future directions for these studies are also discussed.

II. EXPERIMENTAL APPARATUS

A. High-resolution positron beam

Buffer-gas trapping and magnetic beam formation is now an established technique for the creation of a high-resolution positron beam. A brief overview of this process is presented here; recent publications provide a more comprehensive description [28,41].

Positrons are obtained from a ^{22}Na source and moderated using solid neon at a temperature of ~ 7 K. The energy spread of the moderated positrons from the neon is ~ 2 eV, considerably larger than the spread from tungsten moderators which have traditionally been used in positron scattering experiments [12]. However, the efficiency of the moderation process (i.e., the number of moderated positrons per fast positron emitted) is approximately a factor of 10 higher than with typical tungsten moderators [42].

After moderation, the positrons are magnetically guided into a Penning-Malmberg trap, consisting of several cylindrical electrodes in a 0.15 T magnetic field. The electrodes are biased to form a potential well consisting of three stages, as shown in Fig. 1. Successively lower pressures of N_2 gas are maintained in the three stages by differential pumping. In the first stage, with the highest gas pressure, the positrons undergo an inelastic collision with the N_2 , exciting one of the electronic states of the molecule and losing ~ 9 eV in energy. This results in the positrons being trapped in the potential well, where they make successive inelastic collisions and are confined in the third stage in a time of less than 10 ms. In the third stage, positrons cool to room temperature by exciting vibrational and rotational levels of the buffer-gas molecules. A small amount of CF_4 is added to this stage to increase the cooling efficiency by a factor of ~ 10 , as compared to N_2 [43]. The overall efficiency of the trap (i.e., the number of incident low-energy positrons trapped) is as

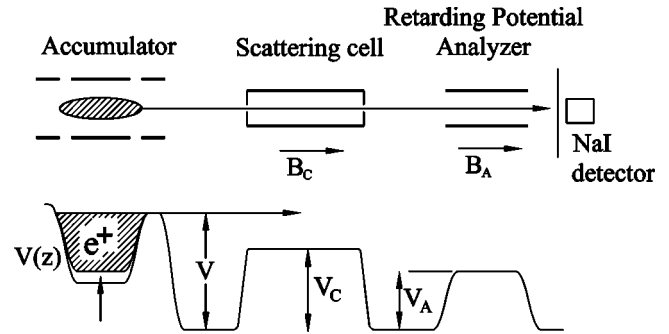


FIG. 2. Positron beam formation and configuration for cross section measurements in a magnetic field. The third stage of the buffer gas trap provides a reservoir of positrons which are released over a well defined potential barrier V . The positrons are then guided magnetically through the gas cell and retarding potential analyzer (RPA). The magnetic fields in the gas cell and RPA, B_C and B_A , respectively, are independently adjustable.

high as 25%. As many as 3×10^8 positrons have been accumulated in 8 min using this method [44].

The trapped positrons can then be used to form a pulsed positron beam by raising the bottom of the confining potential (i.e., stage III of the electrode structure), forcing the positrons over the potential barrier V , as shown in Fig. 2. This procedure creates a beam with a well-defined energy [28]. If appropriate care is taken, the parallel energy spread of the beam can be as low as, or lower than, that of the cooled positron cloud, $\Delta E \leq 0.025$ eV. To achieve this resolution, the number of positrons in the beam is limited by space charge considerations. In practice, $\sim 3 \times 10^4$ positrons are used per pulse, with the pulses having a ~ 3 μs width and a repetition rate of ~ 4 Hz.

B. Scattering cell and beam energy calibration

The positron beam passes through a gas cell that contains the target species. The cell is 38.1 cm long, with an internal diameter of ~ 7 cm and apertures of 5 mm at each end. Construction is from gold-plated copper to provide an electric potential which is as uniform as possible.

In measuring scattering cross sections, the path length and target gas density in the gas cell are two crucial parameters (explained further in Sec. III below). Apertures that are small compared to the internal diameter of the cell create a well-defined region of constant pressure, which falls off quickly at each end. The scattering path length of the positron beam is then taken to be the geometrical length of the cell (i.e., 38.1 cm). Target gas pressures are measured using a capacitance manometer, which has an accuracy of better than 1% when the gas is at a pressure of 0.1 to 1.0 mTorr, typical of the range of pressures for the experiments described here.

Another important consideration is accurate knowledge of the positron beam energy inside the gas cell. In principle, this can be obtained from the voltages V and V_C in Fig. 2. Experience has shown, however, that there can be offsets between the applied and actual potentials on the elements in the system. These offset potentials can be sizable, ranging from 10 meV to tenths of an eV. Several complementary techniques

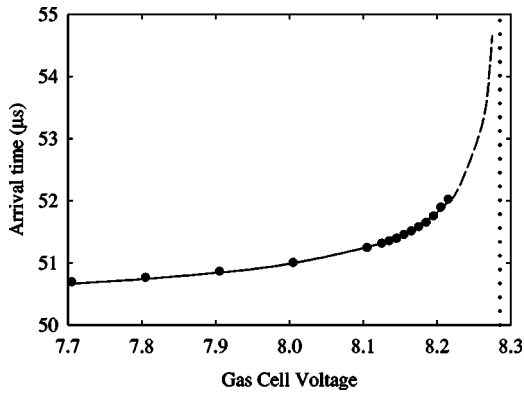


FIG. 3. An example of the timing data and fit used to determine the positron energy in the gas cell as a function of the applied voltage: (●) measured arrival time after a timing trigger; (—) fit to the data; (- - -) extrapolation of the fit; and (⋯) calculated zero energy asymptote from this extrapolation. The fit to this data gives zero energy in the cell at a voltage of 8.285 V. The corresponding cutoff measurement was 8.225 V.

are used to determine the actual beam energy inside the cell. The first is to use the gas cell as an analyzing element, increasing the potential on the cell until the positron beam is cut off. This essentially measures V , and by setting the gas cell voltage relative to this voltage, the energy of the beam in the gas cell is determined. However, in the course of performing the scattering experiments, it was found that there can be discrepancies between the energy set in this fashion and the known threshold for excitation processes (e.g., the onset of vibrational excitation). This was attributed to potential variations in the gas cell, particularly at the ends, where the positron beam passes closest to the material surfaces. The origin of these offsets is not presently understood.

The previously described technique for determining the beam energy by the cutoff potential measures the highest potential along the length of the gas cell. If there is a small region with a higher potential than the rest of the cell, the beam could be at a higher energy for much of the path length through the cell. A different method was then devised to attempt to quantify the maximum deviation of the path-averaged potential from the measured cutoff potential.

The positron beam is pulsed in nature, with each pulse having a typical duration $\sim 3 \mu\text{s}$. The signal from the NaI detector has a corresponding width, and the mean arrival time of the positron pulse can be determined to an accuracy of $\sim 0.1 \mu\text{s}$. As the energy of the positron beam in the gas cell approaches zero, the pulse is delayed due to the longer transit time through the gas cell. Using the potential profile of the gas cell from an electrostatic calculation, the expected delay can be determined as a function of the potential on the gas cell. This delay time was measured as a function of gas cell voltage, and the data were fitted using the appropriate functional form. An example of this is shown in Fig. 3. The key point is that, as the energy of the beam in the gas cell is reduced, the transit time increases, allowing the *average* beam energy in the gas cell to be determined, as well as the potential at which the positron beam is predicted to have zero energy in the gas cell. This “zero energy” voltage was

then compared to the cutoff voltage. The difference between these two potentials is a measure of the maximum potential variation in the gas cell, and therefore is a measure of the quality of a given cell.

Different gas cell designs were tested using this technique before settling on the current version. In this cell design, mesh inserts are placed in the interior of the gas cell near the entrance and exit apertures. The use of mesh combats surface effects by providing a minimal surface area close to the beam which could give rise to stray potentials. The meshes were set at 0.15 V below the gas cell potential, and this effect was taken into account in the analysis of the scattering data. The comparison between the two energy calibration techniques, for this case, showed a difference of 60 meV. This provides an estimate of the uncertainty in the absolute energy calibration of the measurements presented here, although the observed excitation thresholds seem to indicate that the energy is determined to better than this estimate.

III. MEASURING CROSS SECTIONS IN A MAGNETIC FIELD

A. Basic principles

This section describes methods used to study the scattering of positrons from atomic and molecular targets in a magnetic field. Typically, such scattering processes are described in terms of the differential cross section $d^2\sigma(E, E', \Omega)/dE' d\Omega$, such that the intensity I_S of positrons scattered with energy E' into a solid angle $d\Omega$ from an incident beam with intensity I_0 and initial energy E is given by

$$\frac{d^2 I_S}{dE' d\Omega} = n_m l I_0 \frac{d^2 \sigma}{dE' d\Omega}(E, E', \theta), \quad (1)$$

where n_m is the target number density and l is the path length. Assuming unoriented targets, $d\Omega = 2\pi \sin \theta d\theta$, where the scattering angle θ is defined by the velocity vectors of the incident and scattered positrons, \hat{v} and \hat{v}' , respectively, such that $\theta = \cos^{-1}(\hat{v} \cdot \hat{v}')$.

In a conventional scattering experiment (e.g., using an electrostatic beam), the cross section can be measured by measuring the energy E' of the scattered particle into a given solid angle $d\Omega$ at each incident beam energy E and scattering angle θ . However, in the experiments described here, the positrons are confined in a strong magnetic field, so that the small spatial scale of the positron gyromotion makes such a kinematic arrangement impractical. The gyroradius of the positron is given by $\rho = v/\omega_c$, where v is the velocity of the positron and ω_c is the cyclotron frequency. Typical values of ρ in the experiments described here range from a few micrometers to ~ 1 mm. Thus ρ is small compared to both the interaction path length and the size of practically realizable detectors. Consequently, we have pursued a different approach to measure scattering cross sections.

Referring to Fig. 2, the positron beam is magnetically guided through a gas cell, with the energy of the beam in the cell given by $E = e(V - V_C)$. Positrons scattered in the for-

ward direction ($\theta < 90^\circ$) and unscattered positrons are then guided to the retarding potential analyzer (RPA). Positrons scattered in the backward hemisphere ($180^\circ > \theta > 90^\circ$) exit the gas cell, are reflected from the potential wall at the third stage of the buffer-gas trap, and pass through the gas cell once more. Assuming that they make no further collisions (the scattering probability is typically ≤ 0.1), they also travel to the RPA. The strengths of the magnetic fields in the gas cell and RPA are independently adjustable, and this plays a crucial role in the analysis of the scattering processes.

In a magnetic field B , the positron energy E can be separated into a component parallel to the field, E_{\parallel} , and a component perpendicular to the field, E_{\perp} , due to the gyromotion of the positron. The RPA measures only the parallel energy distribution of the beam. Before the scattering event, the initial energy of the positron is such that $E_{\perp} \ll E_{\parallel} \approx E$. In the collision, E is distributed between the internal energy of the target, E_{ex} (i.e., in the case of inelastic scattering), and between E_{\parallel} and E_{\perp} (by scattering through some angle θ) such that $E' = E'_{\parallel} + E'_{\perp} + E_{ex}$. Since the scattering event takes place on a spatial scale much smaller than ρ , it is not substantially altered by the presence of the magnetic field.

While the RPA measures only the E'_{\parallel} distribution of the beam, the ability to change the magnetic field in the RPA relative to the scattering cell enables measurement of the total energy of the scattered particles. In particular, the quantity E_{\perp}/B is an adiabatic invariant in a slowly varying magnetic field. As a result, a change in the magnetic field will change the relative values of E'_{\parallel} and E'_{\perp} . Thus, if we define

$$M = \frac{B_C}{B_A}, \quad (2)$$

where B_C is the field at the gas cell and B_A is the field at the RPA (see Fig. 2), then a reduction in the field of M , reduces E'_{\perp} by the same factor. For $M > 1$, the energy is transferred back into E'_{\parallel} . Consequently, the spread in E'_{\perp} (and E'_{\parallel}) is also reduced by M , and for $M \gg 1$, a RPA measurement provides a direct measure of the total energy distribution of the positron beam. This is discussed further in Sec. III D.

The variables E'_{\parallel} and E'_{\perp} are related to E' and θ by

$$\begin{aligned} E'_{\parallel} &= E' \cos^2 \theta, \\ E'_{\perp} &= E' \sin^2 \theta. \end{aligned} \quad (3)$$

In order to proceed, the scattering cross sections measured as a function of E'_{\parallel} must be related to the standard form for the differential cross section defined in Eq. (1). The relevant differential scattering cross section in the experiments described here is $d^2\sigma(E, E'_{\parallel}, E'_{\perp})/dE'_{\perp}dE'_{\parallel}$ where, in analogy with Eq. (1),

$$\frac{d^2I_S}{dE'_{\perp}dE'_{\parallel}}(E, E'_{\parallel}, E'_{\perp}) = n_m I_0 \frac{d^2\sigma}{dE'_{\perp}dE'_{\parallel}}(E, E'_{\parallel}, E'_{\perp}). \quad (4)$$

The differential cross sections in Eqs. (1) and (4) are related by

$$\frac{d^2\sigma}{dE'd\Omega}(E, E', \theta) = \frac{d^2\sigma}{dE'_{\perp}dE'_{\parallel}}(E, E'_{\parallel}, E'_{\perp})|J|, \quad (5)$$

where $|J| = E' |\cos \theta|/\pi$ is the Jacobian between the variables (E', θ) and $(E'_{\parallel}, E'_{\perp})$.

When the RPA is set to reject $E'_{\parallel} \leq E_A = eV_A$, the beam intensity measured after the RPA will be

$$I_C(E_A) = I_0 - \int_0^{E_A} \frac{dI_S}{dE'_{\parallel}} dE'_{\parallel}, \quad (6)$$

where from Eq. (4)

$$\frac{dI_S}{dE'_{\parallel}}(E, E'_{\parallel}) = I_0 n_m I \frac{d\sigma}{dE'_{\parallel}}(E, E'_{\parallel}), \quad (7)$$

with

$$\frac{d\sigma}{dE'_{\parallel}}(E, E'_{\parallel}) = \int_0^{E'} \frac{d^2\sigma}{dE'_{\parallel}dE'_{\perp}}(E, E'_{\parallel}, E'_{\perp}) dE'_{\perp}. \quad (8)$$

From Eq. (6) we have

$$\frac{dI_C}{dE_A}(E_A) = - \left. \frac{dI_S}{dE'_{\parallel}} \right|_{E_A}. \quad (9)$$

Substituting into Eq. (7) we have

$$\left. \frac{d\sigma}{dE'_{\parallel}} \right|_{E_A} = - \frac{1}{n_m I_0} \frac{dI_C}{dE_A}(E, E'_{\parallel}). \quad (10)$$

Equations (5), (7), (8), and (10) are the basic results, relating a RPA measurement to the conventional differential scattering cross section $d^2\sigma(E, E', \theta)/dE'd\Omega$. We now consider several important special cases.

B. Grand total cross sections

The grand total cross section $\sigma(E)$ can be determined using Eq. (10) so that

$$\begin{aligned} \sigma(E) &= \int_0^E \frac{d\sigma}{dE'_{\parallel}}(E, E'_{\parallel}) dE'_{\parallel} \\ &= - \frac{1}{n_m I_0} \int_0^E \frac{dI_C}{dE_A} dE_A \\ &= \frac{[I_0 - I_C(E)]}{n_m I_0}. \end{aligned} \quad (11)$$

In practice, however, it is not possible to make a measurement of the quantity $I_C(E)$, as this coincides with the cutoff point of the unscattered positron beam. To avoid effects associated with the cutoff, the positron current must be measured at a retarding potential voltage sufficiently offset from the cutoff (i.e., ≥ 3 standard deviations), corresponding to an

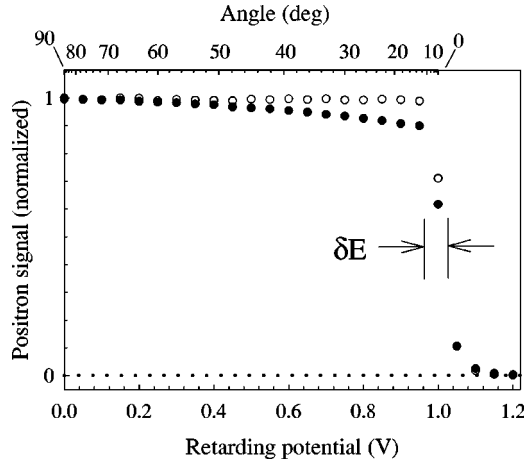


FIG. 4. RPA curve for positron scattering from argon at 1 eV: (●) gas in; (○) gas out. The quantity δE determines the point at which the total cross section is measured (see text). The scattering angles corresponding to the RPA voltages are marked on the upper axis. The differential cross section obtained from this measurement is presented in Fig. 9 below.

energy $E - \delta E$. Thus $I_C(E)$ in Eq. (11) becomes $I_C(E - \delta E)$. This is illustrated in Fig. 4. The open circles in the figure show a measurement of the I_C as a function of RPA voltage with no gas in the scattering cell. It can be seen that the signal is constant until the RPA is at a voltage corresponding to V (see Fig. 1) where there is a sharp drop to zero transmitted current. The width of this step is a measure of the energy resolution of the positron beam, which can be as low as 18 meV. The filled circles show the same RPA measurement when a target gas is present in the cell.

As the RPA voltage is increased, progressively less of the positron beam is transmitted, until it is cut off at a voltage corresponding to the beam energy. The beam resolution in the measurements presented here was 25 meV (FWHM), corresponding to a 3σ value of $\delta E \sim 40$ meV. This restriction means that the measured total cross section excludes some contribution from the differential cross section (DCS). The missing angular range $\delta\theta$, corresponding to δE , can be easily calculated from Eq. (3). Typical values for $\delta\theta$ are shown in Table I. Positrons scattered through angles greater than 90° will be reflected, so that the missing part of the distribution will be 0° to $\delta\theta^\circ$ and $(180 - \delta\theta)^\circ$ to 180° . This missing component must be considered when making comparisons with theory.

C. Differential elastic cross sections

In the case where only elastic scattering is present, $E = E' = E'_\parallel + E'_\perp$. Thus

TABLE I. Approximate angular limits and resolution for selected scattering energies for a beam with an energy resolution of $\Delta E = 25$ meV (FWHM).

Energy (eV)	Upper limit	Lower limit/ $\delta\theta$	Resolution
0.2	69°	26°	$7^\circ - 11^\circ$
1	81°	12°	$1.5^\circ - 5^\circ$
10	87°	4°	$0.15^\circ - 1.5^\circ$

$$\frac{d^2\sigma}{dE' d\Omega}(E, E', \theta) = \frac{d\sigma}{d\Omega}(E, \theta) \delta(E - E'), \quad (12)$$

and

$$\frac{d^2\sigma}{dE'_\perp dE'_\parallel}(E, E'_\parallel, E'_\perp) = \frac{d\sigma}{dE'_\parallel}(E, E'_\parallel) \delta(E - E'_\parallel - E'_\perp). \quad (13)$$

Substituting Eqs. (12) and (13) into Eq. (5) and integrating over E' , we have

$$\begin{aligned} \frac{d\sigma}{d\Omega}(E, \theta) &= \frac{d\sigma}{dE'_\parallel}(E, E'_\parallel) \frac{E \cos \theta}{\pi} \\ &= -\frac{\sqrt{EE'_\parallel}}{\pi n_m I_0} \frac{dI_C}{dE_A}. \end{aligned} \quad (14)$$

The differential cross section can be obtained using the above expression and a RPA measurement of $I_C(E_A)$. An example of such a RPA measurement is shown in Fig. 4. The corresponding cross section for argon is presented below in Sec. IV B.

To make quantitative comparisons with theory, the reflection and retransmission of backscattered particles must be considered. Due to this effect, the measured DCS is actually “folded” around 90° , with the angles θ° and $(180 - \theta)^\circ$ summed. Comparison to theory should then be made by comparing to the theoretical prediction for the same sum.

In the scattering process, the maximum energy that can be transferred from E_\parallel to E'_\perp is the incident beam energy E (i.e., when $\theta = 90^\circ$). Thus the angular information is contained in a region $\Delta V = E/e$ from the RPA cutoff. The practical angular limits and resolution of the measurement can then be determined for a given scattering energy using Eq. (3), namely,

$$\delta\theta = \frac{\delta E'_\parallel}{2\sqrt{EE'_\parallel - E_\parallel^2}}. \quad (15)$$

The energy resolution of the beam (typically, $\Delta E \sim 0.025$ eV) sets the angular resolution. As can be seen from the upper axis of Fig. 4, the angular resolution changes over the range of the RPA measurement, with the best resolution at 45° , and poorer resolution at the limits of the measurement. Close to the beam cutoff, there is also the question of ensuring that there is no contribution to the measurement of I_C from the cutoff, as discussed in Sec. III B. This limits the range of scattering angles which can be studied using this technique. A summary of the limits and resolution for an energy resolution of 25 meV (FWHM) and a variety of incident positron energies is given in Table I.

Two effects are important to consider when measuring the DCS using this method. First, it is necessary to ensure that the gas pressure is such that the probability of multiple scattering is low, since multiple scattering breaks down the one-

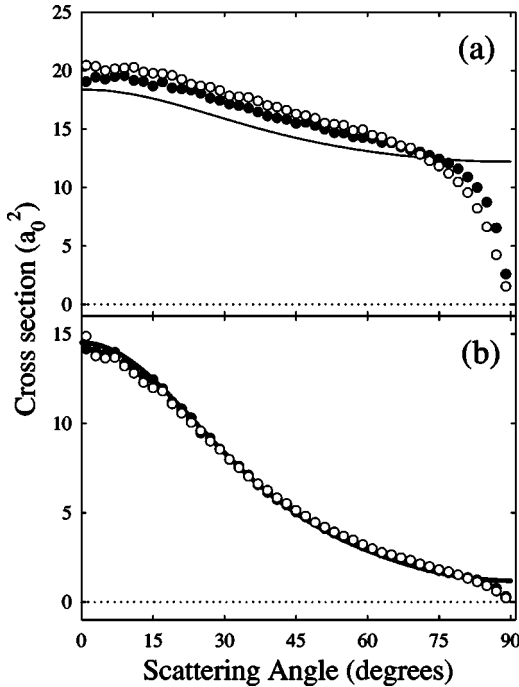


FIG. 5. Monte Carlo simulations of DCS measurements: (a) argon at 0.2 eV incident energy; (b) argon at 1 eV incident energy. Lines are the theory of Ref. [45]; (●) scattering probability of 0.1 in the gas cell; (○) scattering probability of 0.2.

to-one relationship between the RPA voltage and the scattering angle. In addition, particles that lose a substantial amount of E_{\parallel} in a collision will have an increased path length through the gas cell, thus increasing the chance of further scattering. Monte Carlo simulations were performed to assess the extent of these effects. An example of this analysis is shown in Fig. 5. In these simulations, the calculated DCS for positron scattering from argon was used as the initial input [45]. The scattering in the cell was modeled, including the scattering probability and the change in path length introduced by a scattering event. The resulting cross section can then be compared to the input, to investigate the effects of DCS shape and different target gas pressures.

Examples are presented in Figs. 5(a) and 5(b), for argon with incident positrons at 0.2 eV and 1.0 eV, respectively. In both cases, the cross sections were folded around 90° . The cross sections in this and the following figures are given in units of a_0^2 , the square of the Bohr radius. At 0.2 eV, the DCS is underestimated at angles near 90° and overestimated elsewhere. This is due to the increase in path length for particles scattered at angles near 90° (due to the transfer of energy from E_{\parallel} to E_{\perp}), which greatly increases the probability of rescattering. These particles are subsequently scattered back to smaller angles, resulting in a small overestimation of the cross section in this region. The effect is somewhat worse for a higher scattering probability, although the error introduced is no worse than 10% away from the region near 90° in either case. At 1 eV [Fig. 5(b)], the cross section is more forward peaked, and even for a 0.2 scattering probability, there is only a small error introduced in the measurement. It can be seen that there is still a region close to 90° where the

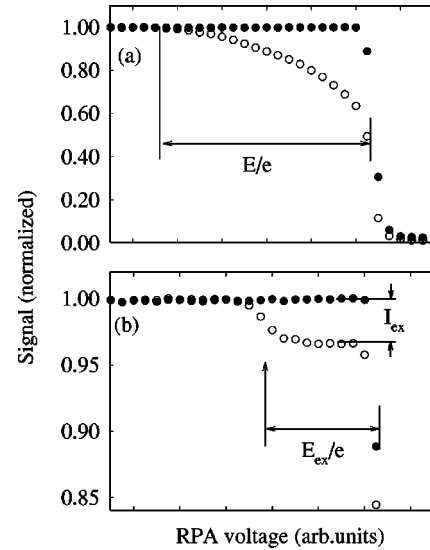


FIG. 6. RPA curves for positrons with 0.5 eV incident energy (○) scattering from CO; and (●) with no gas in the scattering cell: (a) $M=1$, and (b) $M=35$. For $M=35$, a step is apparent at a voltage corresponding to the excitation energy of the vibrational transition in CO. The height of the step is proportional to the total inelastic cross section.

measured cross section is affected, but to a much smaller extent than the previous case.

The results of the simulation provide a measure of the accuracy of this technique in making DCS measurements. If the cross section is forward peaked, errors are small. However, in the case of relatively flat cross sections, near 90° multiple scattering can affect the measurement.

D. Inelastic total cross sections

If there is both elastic and inelastic scattering at a given energy (e.g., a molecular target where the incident energy is above the first vibrational threshold), then for a portion of the scattering $E' \neq E$ and there is no longer a one-to-one relationship between E'_{\parallel} and θ . In the case where the RPA is in the same magnetic field as the gas cell, it is not possible to distinguish between the elastic and inelastic components of the scattering. However, as discussed in Sec. III A, it is possible to take advantage of the fact that E_{\perp}/B is an adiabatic invariant to separate the elastic and inelastic contributions to the scattering. This is illustrated in Fig. 6.

If $M \gg 1$, then at the RPA, $E'_{\parallel} \sim E'$, and thus the distribution of E'_{\parallel} measured will only depend on the total energy loss of the positrons in the collision process. The elastic scattering is reduced to a region close to the cutoff potential, from $(E - \delta)$ to E where $\delta \sim E'/M$. The inelastically scattered portion of the beam will be restricted to a region from $(E - E_{ex} - \delta)$ to $(E - E_{ex} + \delta)$. From Eq. (7),

$$\begin{aligned}
 I_{ex} &= I_C(E - E_{ex} - \delta) - I_C(E - E_{ex} + \delta) \\
 &= n_m I_0 \int_{E - E_{ex} - \delta}^{E - E_{ex} + \delta} \frac{d\sigma}{dE'_{\parallel}} dE'_{\parallel} \\
 &= n_m I_0 \sigma_{ex}.
 \end{aligned}
 \tag{16}$$

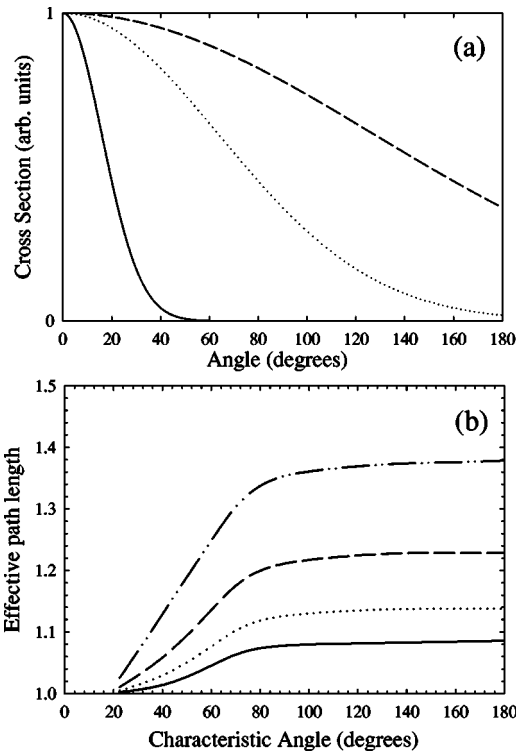


FIG. 7. Monte Carlo simulation to investigate changes in path length due to elastic scattering: (a) sample normalized DCS used in the simulation, with θ_0 of (—) 22.5° , (\cdots) 90° , and (---) 180° ; (b) effect of DCS on the path length for various total scattering probabilities (—) 0.05, (\cdots) 0.1, (---) 0.2, and (— · — ·) 0.4.

Thus

$$\sigma_{ex} = \frac{I_{ex}}{n_m l I_0}. \quad (17)$$

If more than one inelastic channel is open, then a series of steps will appear in the RPA data, corresponding to the various excitations. In this case the cross sections for the separate processes can be determined from a single RPA measurement.

In measuring integral inelastic cross sections, care must be taken to ensure that changes to the scattering path length from the elastic (and other) scattering are small. Typically the largest effect arises from particles scattered elastically, resulting in an increase in their path length, and thus an increased probability of inelastically scattering. This depends on both the gas pressure in the cell and the elastic DCS. To investigate this effect, a Monte Carlo simulation was performed to measure the change in path length for various combinations of DCS and total scattering proportion. The results are shown in Fig. 7. In this case, a model DCS of the form

$$\frac{d\sigma}{d\Omega}(\theta, E) = \sigma_0 e^{-(\theta^2/\theta_0^2)} \quad (18)$$

was used, where θ_0 is a characteristic angle which governs the angular distribution and σ_0 is a constant. Sample cross

sections are shown in Fig. 7(a). These cross sections were used to calculate the effective path length for different total scattering probabilities, with the physical length of the gas cell set to unity.

The results of the simulation are presented in Fig. 7(b). It can be seen that, for forward peaked cross sections (i.e., $\theta_0 \leq 60^\circ$) and scattering probabilities below 0.1, there is less than a 5% increase in the path length for scattering. As the DCS becomes flatter and the scattering probability increases, the correction to the path length becomes greater. For a scattering probability of 0.1, the greatest correction is just below 15%, for the largest value of θ_0 shown. The implications of these results for measuring total inelastic cross sections are that the scattering probability should be kept at 0.1 or less, depending somewhat on the shape of the elastic DCS. It is possible to get a reasonable estimate of the shape of the DCS using the techniques described in Sec. III C, and thus find the appropriate correction factor. With some care, systematic errors due to the underestimation of the path length can be reduced to 10% or less.

E. Positronium formation cross sections

The positronium (Ps) formation threshold for an atom or molecule is given (in electron volts) by $E = E_i - 6.8$, where E_i is the first ionization threshold of the target and 6.8 eV is the binding energy of Ps. Positronium can form in one of two states, ortho- or para-Ps, depending on the relative alignment of the spins of the positron and electron. The ratio of ortho- to para-Ps formation is 3:1. Each state has a different lifetime; for para-Ps it is ~ 125 ps and the Ps molecule decays through 2γ emission with 511 keV/ γ . The lifetime of ortho-Ps is ~ 142 ns, with decay by 3γ emission over a spectrum of energies. At the Ps formation energies of relevance here, para-Ps annihilates within 1 mm of formation, while ortho-Ps formed will either annihilate inside the cell or travel to the walls and annihilate through quenching. A small proportion of the ortho-Ps will be able to travel through the apertures of the gas cell after formation, but will only travel less than 10 cm before annihilating (depending on the kinetic energy of the Ps). The gamma ray detector in the present apparatus is ~ 125 cm from the center of the gas cell, and thus has a solid angle of ≤ 2.8 msr for the detection of gamma rays from Ps annihilation. Only 0.05% of 511 keV γ rays from the annihilation of Ps in the cell will be detected. As a result, it is possible to effectively perform a beam-attenuation experiment to measure the positronium formation cross section. The incident current I_0 can be measured by setting the energy of the positrons in the gas cell below the positronium formation cross section and setting the RPA at 0 V, to allow all scattered and unscattered positrons to pass through the RPA. The proportion of positrons that form Ps with a target atom or molecule at a certain energy can then be determined by setting the energy of the beam in the gas cell to the desired value and measuring the transmitted current I_C (i.e., which will be attenuated due to positronium formation). The cross section is determined in much the same way as the grand total cross section, so that

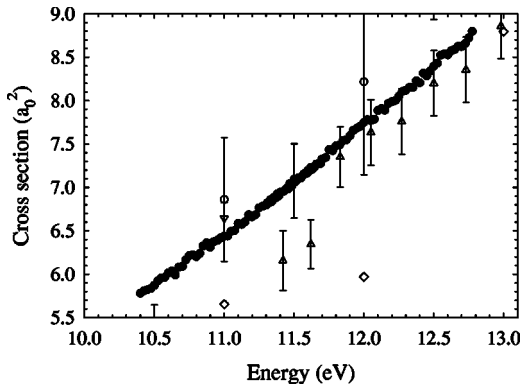


FIG. 8. Grand total cross section for positron scattering from H_2 in the region of the lowest electronic states: (●) present data; (○) Ref. [46]; (△) Ref. [47]; (▽) Ref. [21]; and (◇) Ref. [48]. The absolute error for the present data is $\pm 1.5\%$ on all points. See text for details.

$$\sigma_{Ps} = \frac{1}{n_m l} \frac{I_0 - I_C}{I_0}. \quad (19)$$

Consideration also needs to be given to the increase in effective path length of the positrons through the gas cell, as explained in Sec. III D, and appropriate steps taken to account for this.

IV. RESULTS

In this section, examples of a variety of cross section measurements are presented to demonstrate the applications of the techniques explained above. Contributions to the absolute error in these measurements are estimated to be $\pm 1\%$ from the pressure measurement and $\pm 1\%$ from effects due to variation in the path length. Except where noted, the error is dominated by the statistical uncertainty in the measurements.

A. Grand total cross section for H_2

In Fig. 8, data are presented for the total cross section for positron scattering from H_2 . The major source of error derives from the pressure measurement and corrections for the path length and is $\pm 1.5\%$. Using the technique described in Sec. III B, the measurement was conducted in a search for narrow resonance features [33]. In particular, a strong resonance feature was predicted in the total elastic scattering cross section for H_2 , with a height of $\sim 13 a_0^2$ above the background cross section and an energy width of ~ 8 meV [49]. The fine energy steps in this work demonstrate one of the advantages of using a high-energy-resolution beam to perform positron scattering experiments. There is no evidence of a resonance feature in the experimental data. Given the energy resolution and precision of the experiment, if any resonant feature is present, it is at least a factor of 50 smaller than the theoretical prediction. It is possible for this technique to be used in the search for resonance features in other systems, and some progress has been made in this area [33].

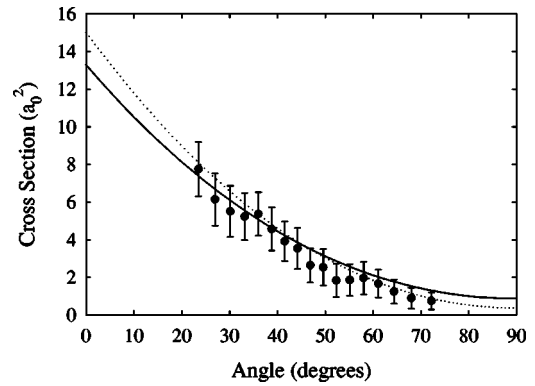


FIG. 9. Differential cross section for positron scattering from argon at an incident energy of 1.0 eV: (●) present data; (—) theory of Ref. [52]; (⋯) theory of Ref. [45]. Both theories have been folded around 90° to compare with the experimental results (see text).

Other candidates for total cross section measurements are experiments at very low impact energies. If reliable cross sections are obtained down to energies < 0.1 eV, it might be possible to extract information about the signs and magnitudes of scattering lengths. This information could be used to assess the possibility of positron bound states. A modified effective range theory analysis has previously been successfully applied in electron scattering [50,51]. However, the problem of the exclusion of part of the angular range in these measurements, especially at low scattering energies, means that improvements will have to be made to the procedure before this is possible for the case of positrons.

B. Differential elastic cross sections for argon and CO

Figure 9 shows absolute DCS measurements for elastic scattering of positrons from argon at an energy of 1.0 eV [30]. Comparison is made with two theories [45,52], and there is good agreement with the data. In these comparisons, the theories are shown folded around 90° , as explained in Sec. III A.

The method described here provides absolute measurements of the elastic DCS for positron scattering from atomic and molecular targets. In a previous experiment, Coleman and McNutt [53] determined the DCS for positron impact on argon, using measurements of the total scattering cross section from another experiment to determine the absolute magnitude. Another difference is that this experiment used a time of flight technique to measure the parallel energy spectrum of the scattered particles, as opposed to the retarding potential analyzer used in the present work. The technique described here (i.e., avoiding timing of individual particles) enables the use of a higher-flux beam. Finally, the cold positron beam employed in the present work permits measurements at much lower values of positron energy than has been possible previously.

Future plans for this type of measurement include extending the measurements to lower energies, where it might be possible to extract information about the sign of the scattering length [45]. This could then also help shed light on the possibility of positron-atom bound states which have been

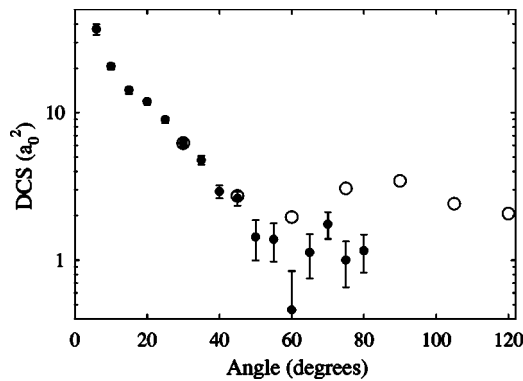


FIG. 10. Differential cross section for positron scattering from CO at an incident energy of 6.75 eV: (●) present data; and (○) relative data of Ref. [23], scaled to the present results at 30°.

calculated and postulated for many systems [36,37,54].

A differential cross section measurement for scattering from CO is shown in Fig. 10. In this case, inelastic scattering is possible, namely, rotational and vibrational excitation (the incident energy is below the lowest electronic excitation for CO). However, previous measurements indicate that the cross sections for vibrational excitation at these energies are very small compared to the total cross section (with a ratio of $\sim 1:25$ [31]); thus nearly all of the scattering is elastic. A comparison is made between the present data for CO and previous measurements of the *relative* elastic DCS for CO [23]. The previous measurements have been scaled to the present data at a scattering angle of 30°. It can be seen that the agreement between the two measurements is reasonably good.

C. Integral inelastic cross sections for CO and Ar

1. CO vibrational excitation

The cross section for excitation of the $\nu=0 \rightarrow 1$ mode by positron impact on CO is shown in Fig. 11 [31]. The data are compared to the available theories for positron scattering from CO [55,56] and experimental data for excitation by electron impact [57,58]. It can be seen that the agreement with the most recent theoretical calculation is excellent over the entire energy range. It has been speculated that the sharp onset is due to a temporary positron resonance [55]. Comparison with the electron data shows the strength of the technique described here for measuring integral cross sections. Typically, for electrons the measurements are done using an electrostatic beam. In this case, the integral cross section for an inelastic process is found by extrapolating and integrating a DCS measurement over the scattering angle. This leads to errors from uncertainty in the extrapolation, as usually not all scattering angles can be measured in the experiment. Since the present technique does not require such a procedure, the error in the determination of the cross section is reduced, as can be seen from Fig. 11.

Measurements of vibrational excitation cross sections by positron impact have been made for several molecular targets [31], and there are plans to extend these measurements. With a change in the detection scheme to charged particle detec-

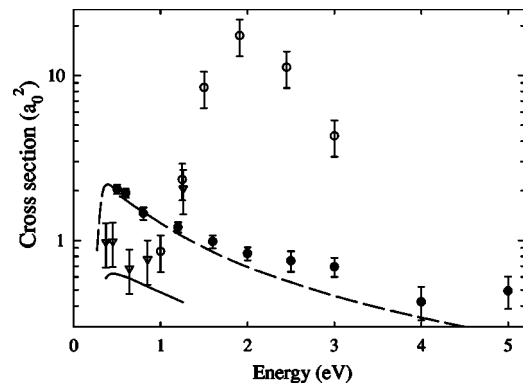


FIG. 11. Integral vibrational excitation cross section for CO by positron impact: (●) present data; (- -) calculation of Ref. [55]; (—) calculation of Ref. [56]. The present data are also compared with cross sections measured for electron impact: (○) Ref. [57] and (▽) Ref. [58]. The precision and accuracy of the present measurements compare favorably to those achieved in electron scattering experiments.

tion (rather than detection of annihilation γ rays), measurements could also be made for electron impact. This would allow a direct comparison, using the same apparatus, of positron and electron scattering cross sections.

2. Ar electronic excitation

Electronic excitation cross sections for positron impact have been measured for a number of targets using the technique described in Sec. III D [32]. To our knowledge, only a few previous measurements of electronic excitation by positron impact have been carried out [15,61–63]. These previous measurements were summed over the entire excitation manifold and thus were unable to discriminate between different final states of the target. The measurements presented here are state-selective cross sections for electronic excitation by positron impact.

In the case of argon, excitation of the $3p^5 4s$ states was investigated. There are four states in this manifold, two associated with each of the two core configurations of $^2P_{1/2}$ ($4s$ $J=0$ and 1) and $^2P_{3/2}$ ($4s$ $J=1$ and 2). Of the four states, only excitation of the two $J=1$ states, can occur by electric dipole excitation. In electron scattering, the $J=0$ and 2 states can be excited through the exchange interaction, but this process is absent for positrons. Thus excitation of the other two states by positron impact can only take place through the spin-orbit interaction. The spin-orbit interaction is expected to be weak for positrons, as the static Coulomb potential is repulsive and there is expected to be little penetration of the incident positron into the target [38,39]. The data presented here support this proposition, as there was no observation of excitation of the $^2P_{1/2} 4s$ ($J=0$) or $^2P_{3/2} 4s$ ($J=2$) levels at any of the energies studied.

The results for the excitation of the two $J=1$ states are shown in Fig. 12. It can be seen that the cross section for the $^2P_{1/2}$ state is somewhat larger than that for the $^2P_{3/2}$ state. The results for electron scattering are also shown [59]. There appears to be agreement between the electron and positron data, although there are somewhat fewer electron data avail-

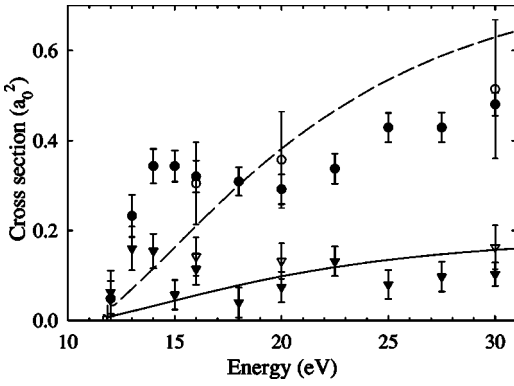


FIG. 12. Cross sections for the electronic excitation of Ar by positron and electron impact. $^2P_{1/2}$ ($J=1$) state: (●) positrons, (○) electrons [59], (---) theory [60]; $^2P_{3/2}$ ($J=1$) state: (▼) positrons, (▽) electrons [59], (—) theory [60].

able. There is good agreement with the relativistic polarized orbital theory of Ref. [60] at energies above ~ 15 eV. The sharp onset and the structure just below 15 eV are not reproduced by the theory, and seem worthy of further investigation.

A comparison of the present results with previous positron experiments is shown in Fig. 13. The previous data are for the cross section summed over all excitation processes, excluding ionization [15,64]. The present data were summed for a comparison to these results. There is reasonable accord with one of the two previous experiments [64], while the other is approximately a factor of 4 larger [15]. Both of the previous measurements exhibit a steep rise at an energy close to the ionization threshold which is not evident in the present measurements.

D. Positronium formation cross section for argon

Positronium formation cross sections for argon have been obtained at the energies where electronic excitations were studied. Figure 14 shows these data and comparisons to previous measurements [18,17], and one theoretical calculation [65]. The absolute error in these data is $\pm 1.5\%$, determined by the pressure measurement and path length corrections.

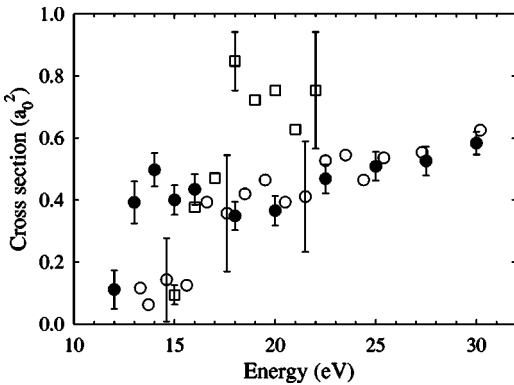


FIG. 13. Electronic excitation of argon by positron impact: (●) present data (summed); (□) Ref. [64]; (○) $0.25 \times$ Ref. [15].

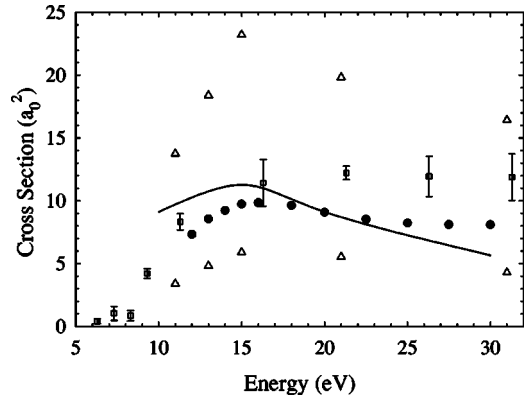


FIG. 14. Positronium formation cross section for positron impact on argon: (●) present data; (Δ) upper and lower limits from Ref. [17]; (□) Ref. [18]; (—) theory of Ref. [65].

The statistical error is small compared to this value. The present results are in good agreement with the theoretical predictions.

These measurements are also in good agreement with the experimental results of Fornari *et al.* [18], in which a similar technique was used to measure the positronium formation cross sections. One difference between the two methods is that the current technique does not require the use of an independent measurement of the total cross section, such as that employed in the Fornari *et al.* experiment.

Future experiments using the technique described here should be able to investigate the behavior near threshold. Other potentially interesting areas of investigation include the possibility of positronium formation involving inner-shell electrons, from targets such as the rare gases, and searches for resonances in the positronium formation channel.

V. FUTURE DIRECTIONS

There are a number of possible extensions and improvements of the experimental techniques described here. One disadvantage of the technique is that particles scattered backward in the gas cell are reflected from the trap potential and pass through the cell again. As explained in Sec. III A, this leads to the indistinguishability of particles scattered at θ° and $(180 - \theta)^\circ$. It should be possible to circumvent this difficulty by the insertion of $E \times B$ deflection plates before the gas cell, which would remove these backscattered positrons from the beam. By making measurements with and without this device, the backscattering and forward scattering could, in principle, both be determined, in order to provide a measurement of the full DCS.

The angular range of the measurements is currently limited by the energy resolution of the beam, as explained in Sec. III B. This hampers measurement of low-energy cross sections, since below about 0.5 eV significant portions of the angular range are inaccessible. A higher-resolution beam would allow measurements at significantly lower energies, where it might be possible to investigate rotational excitations and measure scattering lengths. One possible method to achieve higher resolution is to use filtering techniques on the ~ 25 meV energy resolution beam. This approach has lim-

ited value, however, as any significant improvements to the resolution will come at the cost of positron throughput.

A trap is currently under construction that uses a high magnetic field (~ 5 T) to trap and cool positrons in an electrode structure cooled to temperatures below 10 K [40]. This should allow the formation of a 1 meV positron plasma, and hence provide the opportunity to produce a positron beam with 1 meV energy resolution. In order to conduct such experiments, the stray electrical potentials (i.e., observed on the present generation of scattering cells and described above) must be greatly reduced. Work to accomplish this is currently in progress. Using a 1 meV beam and the scattering techniques described here should enable the investigation of very low-energy positron interactions with matter.

Extensions of the analysis techniques presented here are also planned, including measurement of inelastic DCS and elastic DCS measurements above inelastic thresholds. This could be accomplished using a combination of RPAs, one in a high magnetic field and one in a low magnetic field, or possibly by using a variation of the technique used to measure total inelastic cross sections.

One further extension to the work described above would be to include electron detection for the measurement of electron scattering cross sections. The techniques for positron trapping, beam formation, and measurement of scattering cross sections described here are also applicable for electrons. Studies of electron scattering using these techniques would not only provide a direct comparison between positron and electron data, but might also make a significant contribution to electron scattering in areas where the tech-

niques described here have been shown to have advantages over conventional approaches [26].

VI. CONCLUSIONS

This paper describes several techniques for measuring positron scattering cross sections in a high magnetic field and examples of cross sections measured using these techniques. In conjunction with the high-resolution positron beam ($\Delta E \leq 25$ meV) made available using a buffer-gas positron trap, these techniques have enabled positron scattering experiments with advances in the range of energies studied (down to ~ 0.1 eV), including improved energy resolution and state selectivity. Using these techniques, the details of low-energy positron interactions with matter can be explored with more precision than was possible previously. These measurements present challenges to theory for description of a number of positron-atom and positron-molecule scattering processes.

ACKNOWLEDGMENTS

The authors would like to thank E. A. Jerzewski for his expert technical assistance. We would also like to acknowledge helpful discussions with G. Gribakin, R. McEachran, and M. Lima, as well as thanking them for providing tabulated results, often before publication. S.J.B. would like to thank the Fulbright Association and the University of California, San Diego, for partial support during his time in San Diego. This work is supported by the National Science Foundation, Grant No. PHY 98-786894, and the Office of Naval Research, Grant No. N00014-02-1-0123.

-
- [1] T.S. Stein and W.E. Kauppila, *Adv. At. Mol. Phys.* **18**, 53 (1982).
- [2] M. Charlton, *Rep. Prog. Phys.* **48**, 737 (1985).
- [3] M. Charlton and G. Laricchia, *J. Phys. B* **23**, 1045 (1990).
- [4] W.E. Kauppila and T.S. Stein, *Adv. At., Mol., Opt. Phys.* **26**, 1 (1990).
- [5] G. Laricchia and M. Charlton, in *Positron Beams and their Applications*, edited by P. Coleman (World Scientific, Singapore, 2000), p. 41.
- [6] M. Kimura, O. Sueoka, A. Hamada, and Y. Itikawa, *Adv. Chem. Phys.* **111**, 537 (2000).
- [7] M. Charlton and J. Humberston, *Positron Physics* (Cambridge University Press, New York, 2001).
- [8] *New Directions in Antimatter Chemistry and Physics*, edited by C. M. Surko and F. A. Ginaturco (Kluwer Academic Publishers, Dordrecht, 2001).
- [9] P.J. Schultz and K.G. Lynn, *Rev. Mod. Phys.* **60**, 701 (1988).
- [10] R.G. Greaves and C.M. Surko, *Phys. Plasmas* **4**, 1528 (1997).
- [11] L.D. Hulett, Jr., D.L. Donohue, J. Xu, T.A. Lewis, S.A. McLuckey, and G.L. Glish, *Chem. Phys. Lett.* **216**, 236 (1993).
- [12] P. Coleman, in *Positron Beams and their Applications* (Ref. [5]), p. 11.
- [13] P. Ashley, J. Moxom, and G. Laricchia, *Phys. Rev. Lett.* **77**, 1250 (1996).
- [14] J. Moxom, P. Ashley, and G. Laricchia, *Can. J. Phys.* **74**, 367 (1996).
- [15] S. Mori and O. Sueoka, *J. Phys. B* **27**, 4349 (1994).
- [16] K. Paludan *et al.*, *J. Phys. B* **30**, L581 (1997).
- [17] T.S. Stein, W.E. Kauppila, C.K. Kwan, S.P. Parik, and S. Zhou, *Hyperfine Interact.* **73**, 53 (1992).
- [18] L.S. Fornari, L.M. Diana, and P.G. Coleman, *Phys. Rev. Lett.* **51**, 2276 (1983).
- [19] B. Jin, S. Miyamoto, O. Sueoka, and A. Hamada, *At. Collisions Res. Jpn.* **20**, 9 (1994).
- [20] J. Moxom, G. Laricchia, M. Charlton, A. Kovar, and W. Meyerhof, *Phys. Rev. A* **50**, 3129 (1994).
- [21] S. Zhou, H. Li, W.E. Kauppila, C.K. Kwan, and T.S. Stein, *Phys. Rev. A* **55**, 361 (1997).
- [22] T.S. Stein, J. Jiang, W.E. Kauppila, C.K. Kwan, H. Li, A. Surdutovich, and S. Zhou, *Can. J. Phys.* **74**, 313 (1996).
- [23] D.A. Przybyla, W. Addo-Asah, W.E. Kauppila, C.K. Kwan, and T.S. Stein, *Phys. Rev. A* **60**, 359 (1999).
- [24] H. Gao, A.J. Garner, J. Moxom, G. Laricchia, and A. Kovar, *J. Phys. B* **32**, L693 (1999).
- [25] L. Dou, W.E. Kauppila, C.K. Jwan, and T.S. Stein, *Phys. Rev. Lett.* **68**, 2913 (1992).
- [26] S. J. Buckman, in *New Directions in Antimatter Chemistry and Physics* (Ref. [8]), p. 391.
- [27] T.J. Murphy and C.M. Surko, *Phys. Rev. A* **46**, 5696 (1992).
- [28] S.J. Gilbert, C. Kurz, R.G. Greaves, and C.M. Surko, *Appl. Phys. Lett.* **70**, 1944 (1997).

- [29] C. Kurz, S.J. Gilbert, R.G. Greaves, and C.M. Surko, *Nucl. Instrum. Methods Phys. Res. B* **143**, 188 (1998).
- [30] S.J. Gilbert, R.G. Greaves, and C.M. Surko, *Phys. Rev. Lett.* **82**, 5032 (1999).
- [31] J.P. Sullivan, S.J. Gilbert, and C. Surko, *Phys. Rev. Lett.* **86**, 1494 (2001).
- [32] J.P. Sullivan, S.J. Gilbert, and C. Surko, *Phys. Rev. Lett.* **87**, 073201 (2001).
- [33] J.P. Sullivan, S.J. Gilbert, S.J. Buckman, and C.M. Surko, *J. Phys. B* **34**, L467 (2001).
- [34] K. Iwata, R.G. Greaves, T.J. Murphy, M.D. Tinkle, and C.M. Surko, *Phys. Rev. A* **51**, 473 (1995).
- [35] T.J. Murphy and C.M. Surko, *J. Phys. B* **23**, 727 (1990).
- [36] G.F. Gribakin, *Phys. Rev. A* **61**, 022720 (2000).
- [37] K. Iwata, G. Gribakin, R.G. Greaves, C. Kurz, and C.M. Surko, *Phys. Rev. A* **61**, 022719 (2000).
- [38] W. Raith, in *Photonic, Electronic and Atomic Collisions*, edited by F. Aumayr and H. Winter (World Scientific, Singapore, 1998), p. 341.
- [39] A. D. Stauffer and R. P. McEachran, in *Proceedings of the 3rd International Workshop on Positron (Electron)-Gas Scattering*, edited by W. E. Kauppila, T. S. Stein, and J. Wadehra (World Scientific, Singapore, 1986), p. 166.
- [40] C.M. Surko, R.G. Greaves, K. Iwata, and S.J. Gilbert, *Nucl. Instrum. Methods Phys. Res. B* **171**, 2 (2000).
- [41] S. Gilbert, J. Sullivan, R. Greaves, and C. Surko, *Nucl. Instrum. Methods Phys. Res. B* **171**, 81 (2000).
- [42] A.P. Mills, Jr. and E.M. Gullikson, *Appl. Phys. B: Photophys. Laser Chem.* **49**, 1121 (1986).
- [43] R.G. Greaves and C.M. Surko, *Phys. Rev. Lett.* **85**, 1883 (2000).
- [44] C.M. Surko, S.J. Gilbert, and R.G. Greaves, in *Non-Neutral Plasma Physics III*, edited by J.J. Bollinger, R.L. Spencer, and R.C. Davidson (AIP, New York, 1999), pp. 3–12.
- [45] G. F. Gribakin (private communication) .
- [46] K.R. Hoffman, M.S. Dababneh, Y.F. Hsieh, W.E. Kauppila, V. Pol, J.H. Smart, and T.S. Stein, *Phys. Rev. A* **25**, 1393 (1982).
- [47] M. Charlton, T.C. Griffith, G.R. Heyland, and G.L. Wright, *J. Phys. B* **13**, L353 (1980).
- [48] P.G. Coleman, T.C. Griffith, G.R. Heyland, and T.R. Twoomey, as reported in Hoffman, *et al.* [46].
- [49] M. A. Lima, in *New Directions in Antimatter Chemistry and Physics* (Ref. [8]) p. 493.
- [50] S.J. Buckman and J. Mitroy, *J. Phys. B* **22**, 1365 (1989).
- [51] S.L. Lunt, J. Randell, J.-P. Ziesel, G. Mrotzek, and D. Field, *J. Phys. B* **31**, 4225 (1998).
- [52] R.P. McEachran, A.G. Ryman, and A.D. Stauffer, *J. Phys. B* **12**, 1031 (1979).
- [53] P.G. Coleman and J. McNutt, *Phys. Rev. Lett.* **42**, 1130 (1979).
- [54] J. Mitroy, M.W.J. Bromley, and G. Ryzhikh, *J. Phys. B* **32**, 2203 (1999).
- [55] F.A. Gianturco, T. Mukherjee, and P. Paoletti, *Phys. Rev. A* **56**, 3638 (1997).
- [56] A. Jain, *J. Phys. B* **19**, L379 (1986).
- [57] J.C. Gibson, L.A. Morgan, R.J. Gulley, M.J. Brunger, C.T. Bundschu, and S.J. Buckman, *J. Phys. B* **29**, 3197 (1996).
- [58] W. Sohn, K.H. Kochem, K. Jung, H. Ehrhardt, and E.S. Chang, *J. Phys. B* **18**, 2049 (1985).
- [59] A. Chutjian and D.W. Cartwright, *Phys. Rev. A* **23**, 2178 (1981).
- [60] R. P. McEachran (private communication).
- [61] O. Sueoka, *J. Phys. Soc. Jpn.* **51**, 3757 (1982).
- [62] P.G. Coleman, J.T. Hutton, D.R. Cook, and C.A. Chandler, *Can. J. Phys.* **60**, 584 (1982).
- [63] Y. Katayama, O. Sueoka, and S. Mori, *J. Phys. B* **20**, 1645 (1987).
- [64] P.G. Coleman, T.C. Griffith, and G.R. Heyland, *J. Phys. B* **14**, 2509 (1981).
- [65] M.T. McAlinden and H.R.J. Walters, *Hyperfine Interact.* **73**, 65 (1992).